

Eliminating Registration Bias in Synthetic CT Generation: A Physics-Based Simulation Framework

Lukas Zimmermann^{a,b}, Michael Rauter^c, Maximilian Schmid^{a,b}, Dietmar Georg^{a,b}, Barbara Knäusl^{a,b}

^a*Medical University of Vienna, Department of Radiation Oncology, Vienna, Austria*

^b*Christian Doppler Laboratory for Image and Knowledge Driven Precision Radiation Oncology, Medical University of Vienna, Vienna, Austria*

^c*University of Applied Sciences Wiener Neustadt, Competence Center for Preclinical Imaging & Biomedical Engineering, Wiener Neustadt, Austria*

Abstract

Supervised synthetic Computed Tomography (CT) generation from cone-beam CT (CBCT) requires registered training pairs, yet perfect registration between separately acquired scans remains unattainable. This registration bias propagates into trained models and corrupts standard evaluation metrics. This may suggest that superior benchmark performance indicates better reproduction of registration artifacts rather than anatomical fidelity. We propose physics-based CBCT simulation to provide geometrically aligned training pairs by construction, combined with evaluation using geometric alignment metrics against input CBCT rather than biased ground truth. On two independent pelvic datasets, models trained on synthetic data achieved superior geometric alignment (Normalized Mutual Information: 0.31 vs 0.22) despite lower conventional intensity scores. Intensity metrics showed inverted correlations with clinical assessment for deformably registered data, while Normalized Mutual Information consistently predicted observer preference across registration methodologies ($\rho = 0.31$, $p < 0.001$). Clinical observers preferred synthetic-trained outputs in 87% of cases, demonstrating that geometric fidelity, not intensity agreement with biased ground truth, aligns with clinical requirements.

Keywords: Synthetic CT, Cone-beam CT, Registration bias, Physics-based simulation, Deep learning, Adaptive radiotherapy

1. Introduction

Daily cone-beam computed tomography (CBCT) imaging is the most common used basis for image-guided adaptive radiotherapy (RT) workflows, enabling visualization of daily anatomical changes [1]. However, CBCT images suffer from scatter artifacts, respiratory and organ motion, increased noise, and poor soft tissue contrast compared to fan-beam computed tomography (CT) [2]. These limitations may prevent direct use of CBCT images for critical tasks in adaptive RT such as structure segmentation and dose calculation or introduce systematic uncertainties.

Deep learning approaches have emerged as a promising solution, learning the conversion from CBCT to diagnostic-quality CT (called synthetic CT (sCT)) using paired clinical datasets [3, 4]. This development was further accelerated by large open-source datasets, *e.g.* established through the SynthRAD challenges [5, 6].

However, supervised methods trained on real acquisitions inherit the fundamental limitation that CBCT and CT cannot be registered without residual error [7]. Fan-beam CTs are acquired before treatment under optimal conditions, while CBCTs during the treatment course capture daily anatomy with variations in organ filling, respiratory state, and patient positioning. Even sophisticated deformable image registration (DIR) algorithms cannot achieve perfect correspondence when anatomy has changed between acquisitions [8]. This registration uncertainty creates systematic bias during training. As consequence networks are trained with voxel-wise losses to suppress or blur these features to minimize spatial discrepancies, rather than learning the true intensity transformation while preserving geometric fidelity.

Unpaired learning methods, most notably CycleGAN [9, 10], were developed to circumvent alignment requirements using cycle-consistency losses. While this eliminates the need for paired data, it provides no explicit geometric supervision, allowing hallucination of structures or introduction of artifacts. Recent registration-aware approaches integrate deformable registration networks directly into training [8, 11], but remain dependent on registration quality. Critically, this not only affects training but also evaluation.

Standard intensity metrics measure agreement with ground truth, however, when the ground truth itself contains registration errors, models that reproduce these errors are rewarded. This creates a fundamental evaluation paradox: superior benchmark performance may indicate better learning of registration artifacts rather than better anatomical fidelity. Breaking this

cycle requires both bias-free training data and bias-free evaluation metrics. These considerations also raise the question of suitable evaluation metrics. Current benchmarks rely on intensity-based metrics (Mean Absolute Error (MAE), peak signal-to-noise ratio (PSNR), Structural Similarity index measure (SSIM)) [12], yet for clinical applications requiring accurate image registration, such as dose accumulation, geometric alignment metrics may be at least equally important.

Physics-based simulation offers a different solution. Rather than correcting registration errors or avoiding paired data, simulated CBCT (sCBCT) images generated from fan-beam CT scans are inherently aligned to their source by construction eliminating the registration problem. All image differences arise solely from modeled physical processes rather than anatomical misalignment. Proof of principle studies have explored this direction: DeepDRR demonstrated physics-based X-ray projection synthesis for 2D applications [13] and SinoSynth showed that networks trained on simulated data can outperform those trained on real data [14]. However, extending these concepts to 3D volumetric CBCT synthesis with respiratory motion modeling has not been systematically investigated.

This study presents a physics-based framework for generating sCBCT images from fan-beam CT scans, incorporating heuristic scatter modeling and respiratory motion simulation. Unlike Monte Carlo (MC) simulations, which are computationally prohibitive for large-scale data generation, our approach proved to generate sCBCT images efficiently, enabling creation of training cohorts with guaranteed geometric correspondence. We evaluated this framework in the pelvic region on both a clinical dataset and the SynthRAD 2023 challenge dataset and assessed performance using intensity-based metrics and geometric alignment measures (normalized mutual information (NMI), cross correlation (CC)). This study aims to demonstrate that models trained on simulated imaging data achieve superior geometric alignment compared to models trained on real but imperfectly registered pairs, validating that perfect anatomical correspondence during training enables preservation of spatial relationships.

2. Previous work

Recent registration-aware approaches attempted to address the registration error challenge. Suwanraksa *et al.* developed RegGAN for head and

neck cancer patients, achieving MAE of 43.7 HU by treating imperfect alignment as "noisy labels" [8]. Hu *et al.* proposed SynREG, a transformer-based framework validated across multiple anatomical sites [11]. However, both acknowledged that perfect alignment remains unattainable and hallucinations persist [8, 11]. These findings suggest that attempting to learn and correct for registration errors simultaneously with intensity transformation remains challenging, motivating our approach of eliminating registration errors at the data generation stage.

Physics-based CBCT simulation has been explored previously, though with different objectives and implementation strategies. Peng *et al.* developed SinoSynth, a physics-based degradation model operating in projection (sinoogram) space that demonstrated networks trained on simulated data can outperform those trained on real data [14]. However, the evaluation was performed only for the head and neck region and not for the pelvic area as well as the geometry is a simple fan-beam operating in 2D slices. They describe a random motion model in the form of rotation and resizing the volume not accurately representing physiological deformations. To better simulate breathing motion, which is important in the pelvic region, a physiologically plausible motion model has to be defined.

The DeepDRR framework [13, 15] established foundational methods for physics-based X-ray projection synthesis, demonstrating the feasibility of generating realistic 2D projections for machine learning applications. The GPU-accelerated implementation enables reduced generation times making large-scale dataset creation practical without the computational burden of Monte Carlo simulation. Our work extends these concepts to full 3D volumetric CBCT synthesis while adding respiratory motion modeling.

3. Materials and Methods

3.1. Physics simulation framework

Simulated CBCT images were generated through physics-based simulation of the image acquisition process for the pelvic anatomy. The approach consisted of three sequential stages: (1) respiratory motion simulation to create motion-adapted CT volumes at different breathing phases, (2) forward projection to generate simulated X-ray projections, and (3) reconstruction with simulated artifacts such as scatter, motion, and noise (details in 3.2, 3.3

	Parameter	Value
Motion Simulation	τ_g	200 HU/mm
	bone threshold	200 HU
	T_p	180 ms
	T_{hc}	1.5 s
Dynamic X-ray projection	A_{max}	5 mm
	Φ	$4.16 \cdot 10^5$ photons/(mm ² ·mA·s)
	SPR	1.6
	current	40 mA
	exposure time	40 ms
	detector spacing	0.8 mm × 0.8 mm
	detector size	409.6 mm × 409.6 mm
	detector pixels	512×512
	source-to-detector distance	1536 mm
	source-to-axis distance	1000 mm
	detector offset	115 mm
	start/stop angle	-180/180°
CBCT reconstruction	angle increments	0.54°
	saturation factor	2.0
CBCT reconstruction	volume dimensions (x×y×z)	410 × 410 × 66
	volume spacing (x×y×z)	1 mm×1 mm×4 mm

Table 1: Selected parameters for the simulated image generation. The settings are specific for the Elekta XVI which was clinically available.

and 3.4). An overview of the complete workflow is shown in Figure 1. Scanner specific selected adjustable parameters for our experiments can be found in Table 1. General parameters were fixed and directly stated in the text. The framework can be found at <https://github.com/openvoxelmed/simcbctgenerator>.

3.2. Respiratory Motion Simulation

A motion vector field was derived from the fan-beam CT individually for each patient to simulate abdominal respiratory motion. This field specified a displacement vector for each voxel position, scaled by a time-varying breathing state to generate motion-corrupted volumes representing different phases of the respiratory cycle.

Motion Field Derivation. A heuristic motion field was designed to replicate characteristic abdominal breathing patterns observed during image acquisition. Our respiratory motion exhibits several key assumptions: (1) motion

CBCT Acquisition Workflow with Motion Simulation and Physics

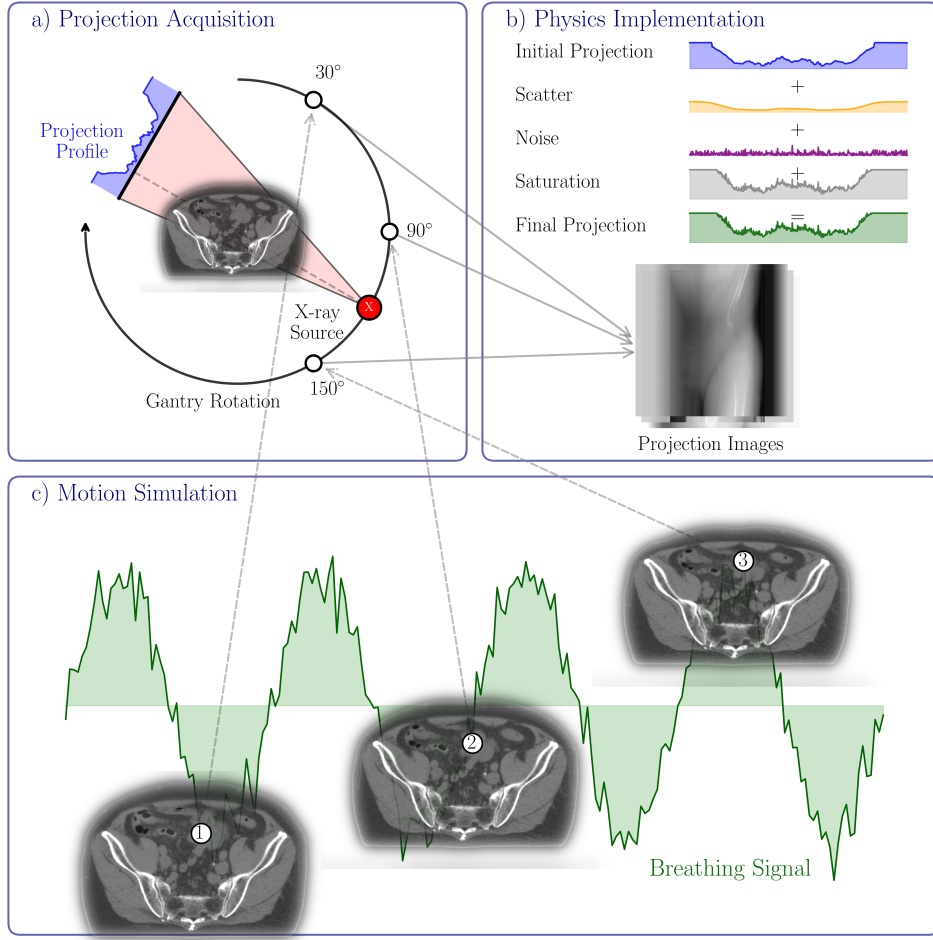


Figure 1: Simulated CBCT generation workflow. The fan-beam CT is deformed using a respiratory motion field to simulate breathing motion (c). Motion-adapted volumes are forward projected to create simulated X-ray projections (a), which are then reconstructed with simulated artifacts (b) to generate the final simulated CBCT.

magnitude is strongest at the patient surface and decreases toward the body center, (2) motion direction aligns with the intensity gradient at tissue-air boundaries (perpendicular to the body surface), (3) motion is predominantly in the anterior direction with increasing attenuation for deviations from this main axis, and (4) motion is minimal in bone regions and tissue posterior to

bone structures.

The motion field generation involved the following steps:

1. Create a binary foreground mask identifying voxels belonging to the patient body and extract the inner boundary of the patient foreground mask to identify the body surface.
2. Compute 3D gradient vectors $\nabla I(\mathbf{x})$ at boundary positions from the CT intensity field, retaining only gradients exceeding the threshold τ_g (Table 1) to create a sparse 3D vector field $\mathbf{V}_s(\mathbf{x})$ (Figure 2a).
3. Propagate boundary gradients throughout the volume using distance-weighted interpolation to create a dense vector field $\mathbf{V}_d(\mathbf{x})$ (Figure 2b).
4. Attenuate motion vectors deviating from the anterior anatomical direction using dot product weighting with the anterior direction vector, where negative dot products are set to zero. The resulting vector field $\mathbf{V}_u(\mathbf{x})$ is shown in Figure 2c.
5. Identify regions requiring strong motion (using a surrogate structure as reference) and regions requiring motion suppression (bone tissue identified by thresholding seen in Table 1, and tissue posterior to bone), which yields the vector field $\mathbf{V}_f(\mathbf{x})$.
6. Apply region-specific attenuation to produce the final motion field $\mathbf{M}(\mathbf{x}, s_i)$, where s_i is the breathing state (see Figure 2d).

Motion-adapted Volume Generation. The breathing state at each X-ray projection is modeled as a sinusoidal function with random perturbations to simulate breathing irregularities:

$$s_i = \sin \left(\pi \frac{i \cdot T_p + \epsilon_i}{T_{hc}} \right) \quad (1)$$

where i is the projection index, T_p is the acquisition time per projection, T_{hc} is the half-cycle breathing period, and $\epsilon_i \sim \mathcal{N}(0, (20 \text{ ms})^2)$ introduces temporal variability in breathing rhythm.

The displacement field at projection i is computed by scaling the motion field with the breathing state and maximum amplitude:

$$\mathbf{D}(\mathbf{x}, i) = A_{max} \cdot \mathbf{M}(\mathbf{x}, s_i) \quad (2)$$

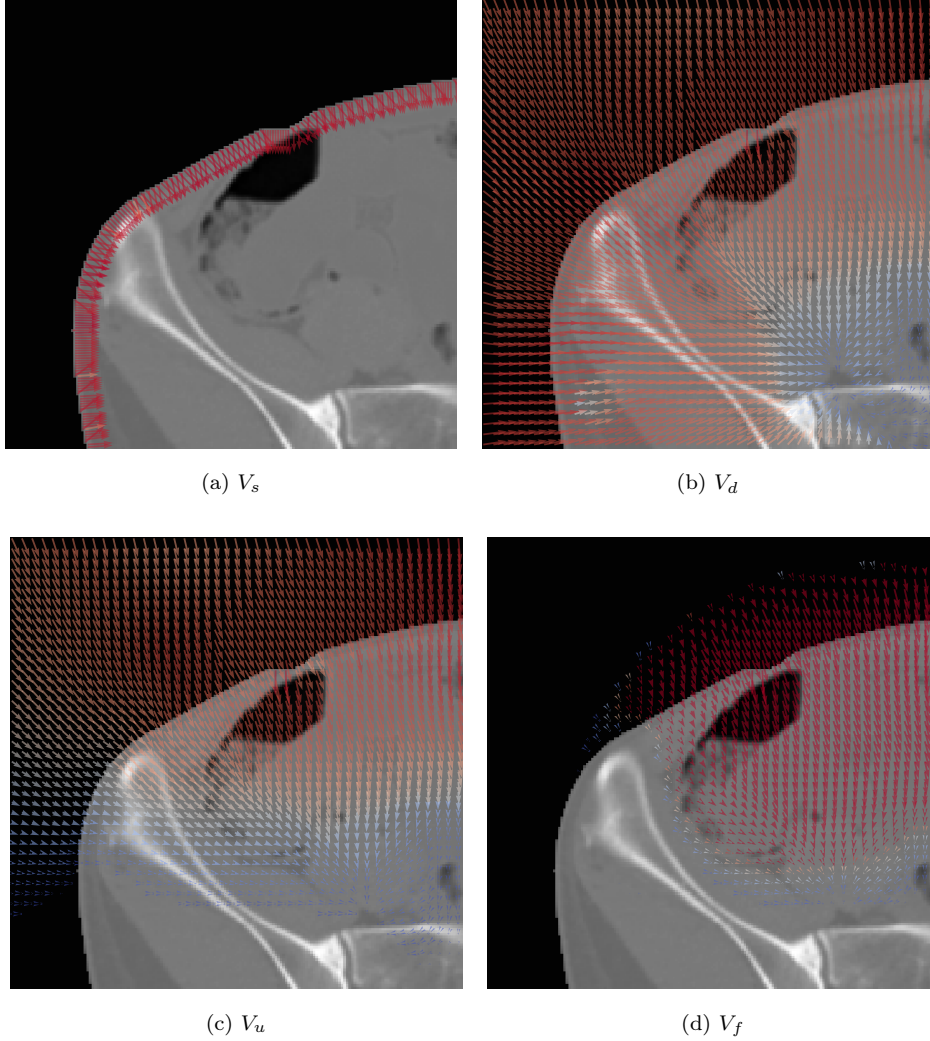


Figure 2: Motion vector field generation (x and y component of 3D motion vector visualized as 2D vector overlay on a central axial slice of test patient volume): the sparse motion vector field (Figure 2a) encodes strong gradient vectors in border voxels, the dense motion vector field (Figure 2b) has a motion vector estimate for every voxel position, the updated motion vector field (Figure 2c) attenuates motion vectors that deviate from the desired main motion direction, and the final motion vector field (Figure 2d) only keeps motion vectors in the extended proximity of the reference structure and eliminating motion vectors at voxels representing bone or voxels behind bones.

The breathing amplitude A_{max} corresponds to $\pm A_{max}$ peak displacement, with $+A_{max}$ representing maximum inhalation and $-A_{max}$ representing max-

imum exhalation. Motion-adapted volumes are generated by resampling the contrast-free CT at positions $\mathbf{x} + \mathbf{D}(\mathbf{x}, i)$ using trilinear interpolation.

3.3. Dynamic X-ray Projection

Our X-ray imaging simulation framework was implemented in CUDA (v12.8) and CuPy, inspired by the DeepDRR package [13], to enable high-performance computation of line integrals through ray casting. The framework incorporated motion-adapted projection capabilities through dedicated CUDA kernels that dynamically resampled the CT volume according to time-varying deformation fields during each projection acquisition.

Contrast Media Removal. Patients often received contrast agent prior to fan-beam CT acquisition for radiotherapy to visualize organs for improved delineation. To simulate CBCT images without contrast enhancement, visible contrast media in the surrogate structure was suppressed. First, a binary mask $M_{binary}(\mathbf{x})$ identified voxels within a predefined segmentation exceeding 50 HU. This mask was convolved with a Gaussian kernel ($\sigma = 1$) to create a fuzzy mask $M(\mathbf{x})$. For each voxel, a noise factor $n(\mathbf{x})$ was sampled from a Gaussian distribution to create smooth intensity transitions:

$$n(\mathbf{x}) \sim \mathcal{N}(1, 0.02^2) \quad (3)$$

The contrast-free CT intensity was computed as:

$$I_{cm-free}(\mathbf{x}) = I_{CT}(\mathbf{x}) - 0.92 \cdot I_{CT}(\mathbf{x}) \cdot M(\mathbf{x}) \cdot n(\mathbf{x}) \quad (4)$$

where the factor 0.92 was empirically determined to best replicate the appearance of non-contrast CT acquisitions. The contrast-free CT was used for all subsequent processing steps.

Scanner Geometry Configuration. The simulation framework is able to replicate cone-beam scanner geometry through configurable acquisition parameters. These included detector dimensions and pixel spacing, source-to-axis and source-to-detector distances, angular sampling density and total rotation arc, as well as detector offset for extended field of view (FOV) configurations. The rotation center can be positioned arbitrarily within the imaging volume, enabling simulation of both standard and offset detector geometries used across different clinical systems. To best represent clinical setup, the isocenter used for the treatment plan can be used as the rotation center. All

scanner specific settings can be found in Table 1

Motion-Adapted Projection Generation. For each projection angle θ_i (where $i = 1, \dots, n$), the CT volume was dynamically resampled according to the time-varying deformation field. The breathing state s_i was computed using Equation 1, and the displacement field (Equation 2) was applied through trilinear interpolation to generate a motion-adapted volume. Ray casting was then performed by defining rays from the X-ray source to individual detector pixels and accumulating attenuation coefficients along each ray path. This dynamic resampling approach ensured that respiratory motion artifacts were properly incorporated into the simulation, providing realistic representation of clinical imaging scenarios where patient motion occurs during the acquisition period.

Physics-Based Imaging Model. Prior to projection, CT Hounsfield unit (HU) values were converted to linear attenuation coefficients using $\mu = \mu_{water} \cdot (\text{HU} + 1000)/1000$ with $\mu_{water} = 0.018 \text{ mm}^{-1}$.

The incident photon distribution at the detector was modeled as:

$$I_0(i, j) = BP(i, j) \cdot mAs \cdot \Phi \cdot p_{size}^2 \quad (5)$$

where $BP(i, j)$ represents a 2D Gaussian beam profile fitted to measured bowtie filter characteristics from the clinical scanner. The beam profile was constructed by computing the mean profile along the longitudinal detector axis and fitting a 1D Gaussian function using scipy's curve fitting. This profile was replicated across the orthogonal axis to create the 2D distribution. The tube current-time product mAs was determined from real measurements (subsection 3.5), Φ is the photon fluence per unit dose, and p_{size} is the detector pixel pitch (see Table 1).

Following the Beer-Lambert law, the attenuation projection $P(i, j)$ was computed through ray casting, and primary transmission was calculated as:

$$T_{primary}(i, j) = \exp(-P(i, j)) \quad (6)$$

yielding primary photon counts:

$$N_{primary}(i, j) = T_{primary}(i, j) \cdot I_0(i, j) \quad (7)$$

Scatter Radiation Model. We implemented a heuristic scatter model that accounts for the spatial distribution of attenuating tissue. First, an attenuation mask was defined to identify regions of significant X-ray absorption:

$$\Omega(i, j) = \begin{cases} 1 & \text{if } T_{primary}(i, j) < 0.5 \\ 0 & \text{otherwise} \end{cases} \quad (8)$$

For each projection, scatter photon counts were estimated using the fifth percentile of primary counts across the detector as a reference level:

$$N_{scatter}(i, j) = SPR \cdot P_5(N_{primary}) \cdot \Omega(i, j) \quad (9)$$

where $P_5(N_{primary})$ denotes the fifth percentile computed over all detector pixels in the current projection, and the scatter-to-primary ratio SPR was empirically set to match clinical CBCT appearance (Table 1).

The multiplication by primary counts ensures that scatter intensity scales appropriately with tissue density.

Noise Model and Projection Finalization. Photon detection noise was modeled using Poisson statistics:

$$N_{detected}(i, j) \sim \text{Poisson}(N_{primary}(i, j) + N_{scatter}(i, j)) \quad (10)$$

The detected photon counts were then normalized by the incident photon distribution, corrected for the detector saturation and converted to logarithmic attenuation space to generate the final noisy projection:

$$P_{noisy}(i, j) = -\ln \left(c_{sat} \cdot \frac{N_{detected}(i, j)}{I_0(i, j)} \right) \quad (11)$$

The saturation constant c_{sat} models the detector's limited dynamic range (Table 1), with the transmission ratio $c_{sat} \cdot N_{detected}/I_0$ clamped to $[10^{-6}, 1.0]$ before applying the logarithm to ensure numerical stability. c_{sat} was selected experimentally according to represent best clinical settings as well as verified via an ablation study (see Appendix A).

3.4. CBCT Reconstruction

Simulated CBCT volumes were reconstructed from the simulated projections using the Feldkamp-Davis-Kress (FDK) algorithm implemented in the Reconstruction Toolkit (RTK) package version 2.7.0 [16]. The reconstruction

used Hann window with cutoff frequency of 0.9 and Truncation correction set to 0.05. The reconstructed volume parameters (dimensions and resolution) can be found in Table 1. The rotation axis was positioned at the treatment planning isocenter to ensure geometric correspondence with the clinical acquisition geometry.

Following reconstruction, gray values were converted to HU using the conversion formula $\mu \times 65536 - 1024$. Regions outside the field of view were identified using a cone-shaped mask determined by the scanner geometry and set to -1024 HU.

Reference CT Preparation. For each sCBCT, the corresponding fan-beam CT was resampled to the same reference space ($410 \times 410 \times 66$ voxels, $1 \text{ mm} \times 1 \text{ mm} \times 4 \text{ mm}$) and truncated using the identical FOV mask. This created perfectly geometrically aligned sCBCT/CT pairs.

3.5. Patient cohort

Clinical dataset. Imaging data from 395 gynecological patients treated at the Department of Radiation Oncology at the Medical University of Vienna between 2022 and 2024 were included. Each patient dataset encompassed CT and CBCT images as well as DICOM structure files including organs and target volume segmentations, and the treatment plan. For patient inclusion, bowel bag delineation was required as surrogate structure elaborated in more detail in subsection 3.2. All CBCT scans were acquired using an X-ray volumetric imaging (XVI) system (Elekta AB, Stockholm, Sweden). The CT scans were acquired using a Siemens Somatom Definition AS scanner (Siemens Healthineers, Germany). This study was approved by the institutional ethics committee (approval number: 1359/2025).

All 395 CT images were used to generate sCBCT/CT pairs using the isocenter extracted from the radiotherapy treatment plan to position the patient according to clinical treatment geometry. For our experiments, we replicated the Elekta XVI system in medium FOV configuration using the settings defined in Table 1. For evaluating model performance on CBCT data, a subset of 180 patients with CBCT scans was selected as training data. These CBCT/CT pairs required spatial alignment. The clinically approved CBCT positioning was used as the initial alignment, followed by deformable registration performed with the Elastix registration tool [17]. For deformable registration, we employed the IMPACT loss metric [18], which uses a pretrained deep learning model (Total Segmentator, M730) as a feature extractor. The

metric compares feature maps from two network layers using L2 distance. Registration parameters included a grid spacing of 16 mm and two resolution layers. An additional 30 patients with CBCT scans were designated as a held-out test set and underwent the same registration procedure.

SynthRAD dataset. Additionally, the SynthRAD Challenge 2023 dataset was included [12]. All available CT scans in the pelvic region were reviewed, and unsuitable images (CT scans with insufficient FOV for motion simulation) were excluded, resulting in 349 patients from which sCBCT/CT pairs were generated. Since the SynthRAD dataset does not include bowel bag delineations required for motion simulation (subsection 3.2), we trained a segmentation model to generate these labels. An nnUNet model with medium sized ResNet encoder and default configuration was trained on the clinical dataset, where bowel bag contours were available from clinical practice. This model was then applied to segment bowel bag structures in the SynthRAD CT images. All predicted segmentations were visually reviewed and manually corrected by a data scientist to ensure anatomical accuracy before use in the simulation pipeline. The dataset includes a variety of gender and tumor types. As the isocenter was not available for these patients, the image center was used as the rotation center for physics simulation. 180 rigidly registered CBCT/CT pairs were used as provided by the challenge organizers. The challenge validation set of 30 patients in the pelvic region was used as an additional held-out test set for our study and is referred to as such throughout this manuscript.

Table 2 summarizes the dataset composition for both simulated and real data configurations.

	simulated CBCT	real CBCT	
	training/validation	training/validation	test
SynthRAD	349	180	30
Clinical	395	180	30

Table 2: Dataset composition showing sample sizes for the SynthRAD Challenge dataset and clinical data, all in the pelvic region. Training data was split into five folds for cross-validation following nnUNet conventions. All planning CT images were used to generate sCBCT/CT pairs, while real CBCT/CT pairs represent subsets with acquired CBCT scans.

3.6. Model training

For all experiments, Nvidia A100 GPUs of the high performance cluster at the Medical University of Vienna were utilized. The regression performance was analyzed in the context of CBCT-to-CT translation. For all runs, a modified nnUNet regression trainer was implemented and used with ResNet encoder configuration medium size, deep supervision loss enabled and L1 loss [19]. The input CBCT images were normalized using Z-scoring and the CT labels were normalized using a global normalization where the mean and standard deviation over the full training dataset were recorded and used during training and inference for normalization and renormalization.

Five-fold cross-validation was performed for both the SynthRAD and clinical datasets. The models were trained for 1000 epochs with a learning rate of 0.01 and the SGD optimizer including Nesterov momentum set to 0.99. Three training configurations were evaluated: (1) $M_{\text{simulated}}$: trained from scratch on synthetic sCBCT/CT pairs generated from real CT images using physics simulation (subsection 3.1), (2) M_{real} : trained from scratch on aligned CBCT/CT pairs, and (3) M_{finetune} : initialized with weights pretrained on synthetic data, then finetuned on real CBCT/CT pairs.

For M_{finetune} , a model was first pretrained on all available simulated data to create an initial checkpoint. Subsequently, the encoder portion of this pretrained model was frozen during finetuning, while the decoder was trained for 50 epochs with a reduced learning rate of 0.001 on the real data from each fold. All other hyperparameters remained identical to the initial training. For evaluation, predictions from all five folds were ensembled by averaging. Performance metrics were reported on the separate held-out test sets consisting of 30 cases each from the SynthRAD and clinical datasets.

3.7. Evaluation

The realism of sCBCT images was evaluated using Fréchet Inception distance (FID) and Maximum Mean Discrepancy (MMD) metrics. FID was computed using an Inception v3 model as the feature extractor, while MMD utilized ViT-L/16 (both accessed from torchvision v0.25.0). 3D images were converted to 2D transversal slices for metric computation. Metrics were calculated separately for simulated data generated from the SynthRAD and clinical datasets. As reference baselines, we also report FID and MMD metrics (1) between SynthRAD and clinical data, and (2) between two equal splittings of the same dataset (called from now on internal FID and MMD

metrics), to provide expected value ranges for interpretation.

For the CBCT-to-CT translation task, we evaluated MAE, SSIM, and PSNR. To test if the output preserves geometric correspondence with the actual geometric anatomy, additionally NMI and CC between predicted synthetic CT (sCT) and the input CBCT were computed. These metrics measure whether the output preserves geometric correspondence with the actual imaged anatomy, independent of ground truth quality. All metrics were computed within an outline mask as defined for the SynthRAD Challenge 2023 to ensure comparability [12]. The mask was defined by an Otsu threshold with different morphological operations. Statistical comparisons between model configurations were performed using the Wilcoxon signed-rank test. To account for multiple comparisons across the five metrics, Bonferroni correction was applied. Effect sizes were quantified using Cohen’s d with interpretation thresholds of $|d| < 0.2$ (negligible), $0.2 \leq |d| < 0.5$ (small), $0.5 \leq |d| < 0.8$ (medium), and $|d| \geq 0.8$ (large).

To complement quantitative metrics and mitigate potential selection bias, a Image Quality scale (IQS) analysis was conducted by five independent observers (Data scientists, Medical physicists, Radiation technologists). Observers evaluated clinical ($n=30$) and SynthRAD ($n=30$) testset predictions from $M_{\text{simulated}}$ and M_{real} using a custom visualization tool that displayed the original CBCT alongside both reconstructed CT volumes with synchronized crosshair navigation. Each observer scored both reconstructions on a scale from 0 (very poor) to 5 (excellent) based on anatomical accuracy, image quality, artifact severity, and overall reconstruction fidelity. Additionally, observers indicated their preference: (1) prefer $M_{\text{simulated}}$, (2) prefer M_{real} , or (3) no preference. The inter-rater consistency was evaluated using Randolph’s Kappa test as well as intraclass correlation coefficient (ICC) for analyzing consistency (two-way mixed effects, average rater). The IQS was designed to validate whether geometric alignment corresponds to clinical perception of quality. Therefore, we performed a correlation analysis between all metrics and the mean IQS over all observers using Spearman’s Rank correlation analysis reporting p-value and the 95% confidence interval (CI95%). Additionally, a Steiger’s Z test was performed comparing the correlation dependency (*e.g.* $\rho(\text{NMI, IQS}) > \rho(\text{MAE, IQS})$).

All statistical analyses were performed using Python 3.12.3 (pingouin v0.5.5).

4. Results

4.1. Simulation Realism

Table 3 presents the FID and MMD scores evaluating simulated CBCT quality. For the SynthRAD dataset, simulated data achieved comparable distribution metrics to the data split comparison of the same dataset (FID: 63.4 vs 52.73; MMD: 0.69 vs 1.07), indicating that simulated images captured the statistical properties of real CBCT data. The clinical dataset demonstrated lower FID scores overall (synthetic: 22.46; internal: 7.73), suggesting more homogeneous imaging characteristics. While the simulated-to-real gap appeared larger for clinical data, the cross-dataset comparison between real SynthRAD and real clinical data (FID: 42.78, MMD: 0.85) demonstrated that distribution differences across datasets can be substantial even among real acquisitions. Further, computing the intensity metrics on the sCBCT/CT pair of the validation sets resulted in 6.7 HU (MAE), 47.1 dB (PSNR) and 0.99 (SSIM) for all 395 Patients of the clinical dataset. sCBCT image generation took approximately 10s per 10M voxel dataset.

Dataset	Comparison	FID ↓	MMD ↓
SynthRAD	simulated vs. real	63.43	0.69
	internal (real vs. real)	52.73	1.07
Clinical	simulated vs. real	22.46	0.68
	internal (real vs. real)	7.73	0.06
SynthRAD vs. Clinical (both real)		42.78	0.84

Table 3: FID and MMD scores evaluating simulated CBCT quality. Lower values indicate more similar distributions. "Simulated vs. real" compares generated images to real acquisitions within each dataset. "Internal" compares two subsets of real data within each dataset. The cross-dataset comparison shows distribution differences between real SynthRAD and clinical data.

4.2. Model Performance

Table 4 presents comprehensive evaluation results across all training and testing configurations. The results demonstrated that models trained on synthetic data ($M_{\text{simulated}}$) consistently achieved superior or equivalent geometric alignment compared to models trained on real data (M_{real}), as measured by

NMI and CC.

A systematic discrepancy emerged between intensity-based and geometric metrics. M_{real} achieved lower MAE (34.76 vs 48.48 HU) when evaluated against ground truth, yet $M_{\text{simulated}}$ demonstrated better geometric alignment with the input CBCT (NMI: 0.30 vs 0.28, CC: 0.98 vs 0.97). The effect was most pronounced in cross-dataset evaluation (models were trained on rigidly aligned data but tested on deformable registered data), where $M_{\text{simulated}}$ improved NMI by 41% relative to M_{real} (0.31 vs 0.22), indicating that registration methodology differences between training and test amplify bias effects.

Performance patterns varied by train-test dataset configuration (Table 4). When both used the same registration methodology, M_{real} achieved lower MAE; when registration methodologies differed, $M_{\text{simulated}}$ achieved lower MAE. For models trained on rigidly registered SynthRAD data and tested on deformably registered clinical data, $M_{\text{simulated}}$ improved MAE by 32.68 HU (39% reduction), PSNR by 4.60 dB, and SSIM by 0.06 compared to M_{real} . Finetuning synthetic-pretrained models on real data (M_{finetune}) yielded performance approaching that of M_{real} , suggesting that synthetic pretraining provides useful initialization that can be refined with limited real data.

Figure 3 provides qualitative visualization of the geometric alignment advantage, showing local NMI heatmaps for $M_{\text{simulated}}$ and M_{real} predictions on SynthRAD test case 2PA020. $M_{\text{simulated}}$ demonstrated consistently higher alignment throughout the anatomy, particularly in anatomically complex regions.

4.3. Observer assessment

The IQS conducted with five independent observers (total evaluations across all test cases) strongly favored outputs from $M_{\text{simulated}}$. Observers preferred $M_{\text{simulated}}$ in 87% of cases, with an average quality rating of 3.94 compared to 2.04 for M_{real} . No clear preference was expressed in 8.8% of cases, while M_{real} was preferred in only 4.2% of cases. Preferences had substantial agreement (Clinical and SynthRad: $\kappa=0.62$). Inter-rater reliability metrics (Table 5) show poor values for both datasets and models comparing the observer scores. For both datasets, $M_{\text{simulated}}$ was more consistent in the rating than M_{real} .

Table 4: Regression Performance: Clinical vs SynthRAD for all Training and Testing dataset combinations. Values depicted are the median with the 25th and the 75th percentiles in brackets. Best performing configuration is marked in bold per metric and combination (training and test dataset). Asterisk mark significant results and ES gives Cohen’s D effect size to $M_{\text{simulated}}$. As reference, SynthRAD challenge winner metrics for the pelvic dataset is also shown.

Test Dataset	Training Data	Model Type	MAE (HU) ↓	PSNR (dB) ↑	SSIM ↑	NMI ↑	CC ↑
Clinical	M _{simulated}	median	48.48	30.17	0.89	0.30	0.98
		IQR	(43.79, 54.81)	(29.22, 30.83)	(0.88, 0.90)	(0.29, 0.32)	(0.97, 0.98)
	M _{real}	median / ES	34.76* / 0.80	31.43* / -0.84	0.93* / -0.95	0.28* / 1.08	0.97* / 0.29
		IQR	(31.23, 40.22)	(30.42, 33.72)	(0.91, 0.94)	(0.26, 0.30)	(0.97, 0.98)
	M _{finetune}	median / ES	37.70* / 0.70	31.40* / -0.81	0.93* / -0.86	0.29* / 0.90	0.98* / -0.06
		IQR	(33.39, 42.04)	(30.34, 33.43)	(0.91, 0.94)	(0.27, 0.30)	(0.97, 0.98)
SynthRAD	M _{simulated}	median	50.56	29.96	0.89	0.31	0.98
		IQR	(44.69, 57.11)	(29.15, 30.66)	(0.88, 0.90)	(0.29, 0.32)	(0.96, 0.98)
	M _{real}	median / ES	83.24* / -2.21	25.36* / 3.44	0.83* / 1.68	0.22* / 3.71	0.87* / 3.87
		IQR	(80.94, 88.89)	(25.09, 25.62)	(0.80, 0.84)	(0.19, 0.23)	(0.81, 0.88)
	M _{finetune}	median / ES	79.72* / -2.06	25.90* / 2.97	0.84* / 1.53	0.23* / 3.39	0.89* / 3.64
		IQR	(78.29, 86.29)	(25.65, 26.35)	(0.81, 0.84)	(0.21, 0.24)	(0.84, 0.90)
SynthRAD	M _{simulated}	median	81.55	26.63	0.83	0.29	0.96
		IQR	(66.79, 86.88)	(25.81, 27.97)	(0.81, 0.85)	(0.27, 0.33)	(0.95, 0.97)
	M _{real}	median / ES	77.61* / 0.01	26.43* / 0.16	0.84* / -0.02	0.27* / 0.95	0.96* / 0.09
		IQR	(69.61, 82.40)	(25.98, 27.66)	(0.82, 0.84)	(0.26, 0.28)	(0.95, 0.97)
	M _{finetune}	median / ES	80.87* / -0.11	26.35* / 0.25	0.83* / 0.09	0.27* / 0.74	0.96* / -0.07
		IQR	(70.68, 87.15)	(25.79, 27.08)	(0.82, 0.85)	(0.26, 0.29)	(0.95, 0.97)
SynthRAD	M _{simulated}	median	77.09	26.83	0.84	0.29	0.96
		IQR	(61.26, 87.67)	(26.08, 28.40)	(0.82, 0.86)	(0.27, 0.33)	(0.95, 0.97)
	M _{real}	median / ES	53.16* / 1.35	29.51* / -1.36	0.88* / -1.22	0.25* / 1.37	0.91* / 1.51
		IQR	(46.39, 63.05)	(28.19, 30.51)	(0.86, 0.90)	(0.20, 0.27)	(0.82, 0.94)
	M _{finetune}	median / ES	57.00* / 1.19	29.48* / -1.34	0.87* / -1.10	0.25* / 1.50	0.90* / 1.53
		IQR	(51.86, 68.26)	(27.94, 30.19)	(0.85, 0.89)	(0.20, 0.27)	(0.83, 0.95)
	challenge	median	49.27	31.02	0.91	-	-
	winner	IQR	(40.81, 55.94)	(29.36, 32.47)	(0.87, 0.94)	-	-

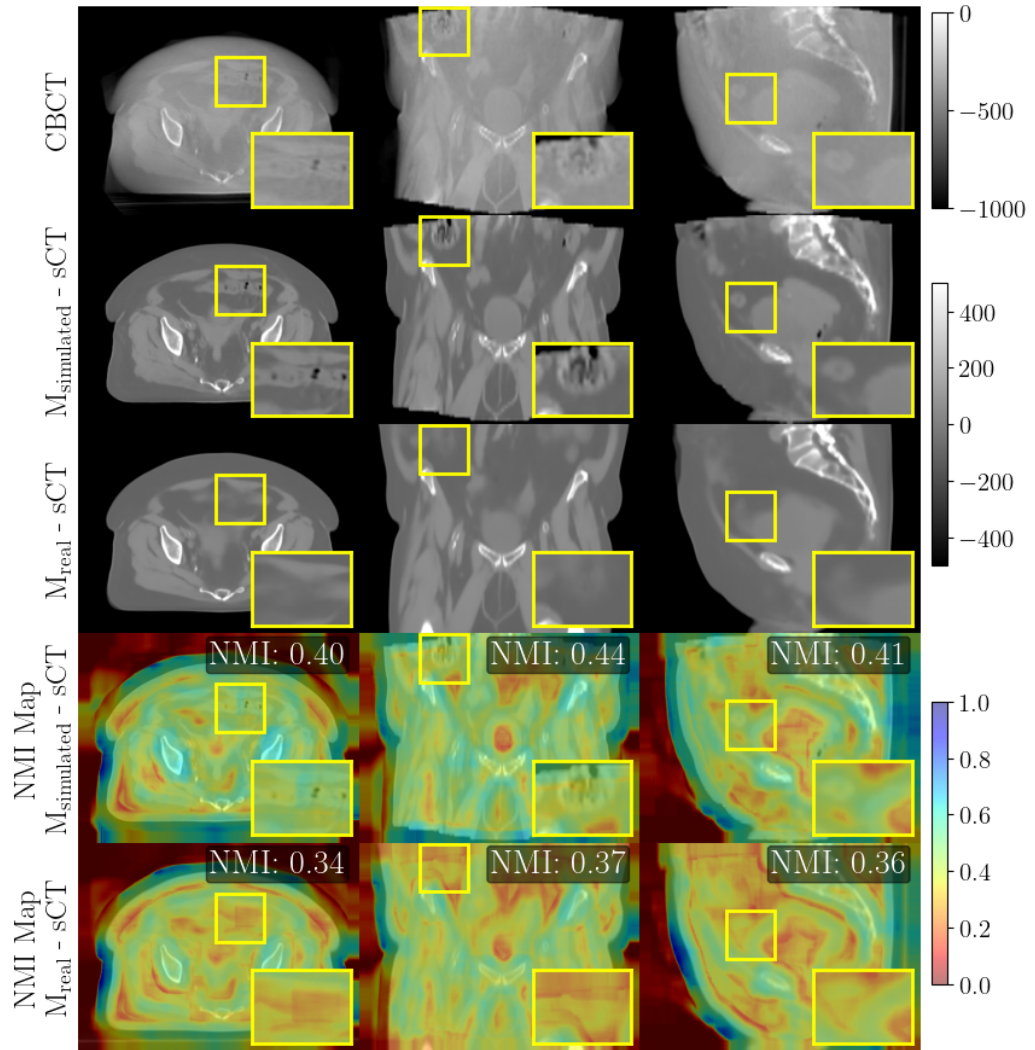


Figure 3: Qualitative comparison of geometric alignment between $M_{\text{simulated}}$ (second row) and M_{real} (third row) visualized using local NMI heatmaps for SynthRAD test case 2PA020. Higher values (blue regions) indicate stronger local alignment with the source CBCT. $M_{\text{simulated}}$ demonstrates superior alignment throughout the volume, particularly in anatomically complex regions.

Dataset	Model type	κ	ICC
Clinical	$M_{\text{simulated}}$	0.18	0.30
	M_{real}	0.12	0.19
SynthRAD	$M_{\text{simulated}}$	0.19	0.45
	M_{real}	0.05	0.24

Table 5: Comparison of inter-rater reliability metrics, Randolph’s kappa (κ) and the intraclass correlation coefficient model ICC, for ratings derived from $M_{\text{simulated}}$ and M_{real} on SynthRAD and Clinical datasets.

Metric	Dataset	ρ	CI95%	p-value
MAE	Clinical	0.57	[0.37, 0.71]	<0.001
	SynthRAD	-0.10	[-0.36, 0.19]	0.45
	Combined	0.02	[-0.16, 0.22]	0.80
PSNR	Clinical	-0.46	[-0.63, -0.25]	<0.001
	SynthRAD	0.16	[-0.15, 0.41]	0.23
	Combined	0.03	[-0.17, 0.22]	0.75
SSIM	Clinical	-0.59	[-0.72, -0.40]	<0.001
	SynthRAD	0.10	[-0.16, 0.36]	0.43
	Combined	-0.05	[-0.24, 0.14]	0.58
NMI	Clinical	0.29	[0.04, 0.52]	0.02
	SynthRAD	0.31	[0.06, 0.54]	0.02
	Combined	0.31	[0.14, 0.45]	<0.001
CC	Clinical	0.06	[-0.20, 0.31]	0.65
	SynthRAD	-0.06	[-0.28, 0.18]	0.67
	Combined	0.05	[-0.14, 0.22]	0.62

Table 6: Spearman correlation between image quality metrics and clinical assessment (IQS), stratified by dataset and combined. n=60 per dataset, n=120 combined.

The computed Spearman correlations between per-case metric values and mean IQS across observers can be found in Table 6. A divergence emerged between datasets with different registration methodologies which can be seen in Figure 4.

For the clinical dataset (deformable registration), intensity metrics exhib-

ited strong but inverted correlations with clinical assessment. Higher MAE correlated with higher IQS ($\rho = 0.57$, $p < 0.001$), while higher PSNR and SSIM correlated with lower IQS ($\rho = -0.46$ and $\rho = -0.59$, respectively, both $p < 0.001$). This inversion indicated that outputs achieving better intensity metrics were systematically rated as clinically inferior by observers.

For the SynthRAD dataset (rigid registration), intensity metrics showed no significant correlation with IQS (all $p > 0.2$).

In contrast, NMI demonstrated consistent positive correlation with IQS across both datasets (clinical: $\rho = 0.29$, $p = 0.02$; SynthRAD: $\rho = 0.31$, $p = 0.02$), confirming its validity as a predictor of clinical preference independent of ground truth quality. CC showed no significant correlation in either dataset. When datasets were combined, intensity metric correlations were small and not significant and only NMI showed moderate correlation ($p < 0.001$). Steiger's Z tests confirmed that NMI predicted IQS significantly better than MAE ($Z = 2.27$, $p = 0.02$) and SSIM ($Z = 2.53$, $p = 0.01$) in the combined analysis.

5. Discussion

In our study, a computational efficient framework for simulated CBCT generation including heuristic scatter modeling, analytic motion field simulation, and optimized CUDA kernels was successfully implemented. This enabled practical large-scale dataset generation without the requirement of aligned CT-CBCT pairs. We demonstrated that the framework is capable to create realistic images which were used to perform a systematic comparison between models trained with real and simulated data.

Our results revealed a fundamental tension in supervised sCT evaluation. Standard benchmark metrics reward registration bias reproduction: Models trained on real data (M_{real}) achieved lower MAE precisely because they learned to replicate the spatial errors present in imperfectly registered training pairs. This effect was configuration-dependent. When training and test datasets shared the same registration methodology, networks optimizing for biased ground truth were rewarded, and M_{real} achieved superior intensity metrics. However, when registration quality differed between training and testing, this learned bias became misaligned with the test distribution, and $M_{\text{simulated}}$ demonstrated advantages in both geometric alignment and intensity metrics. This might occur when externally trained models are deployed at new institutions with significant implications: challenge leaderboards ranking methods by MAE or SSIM may systematically favor biased

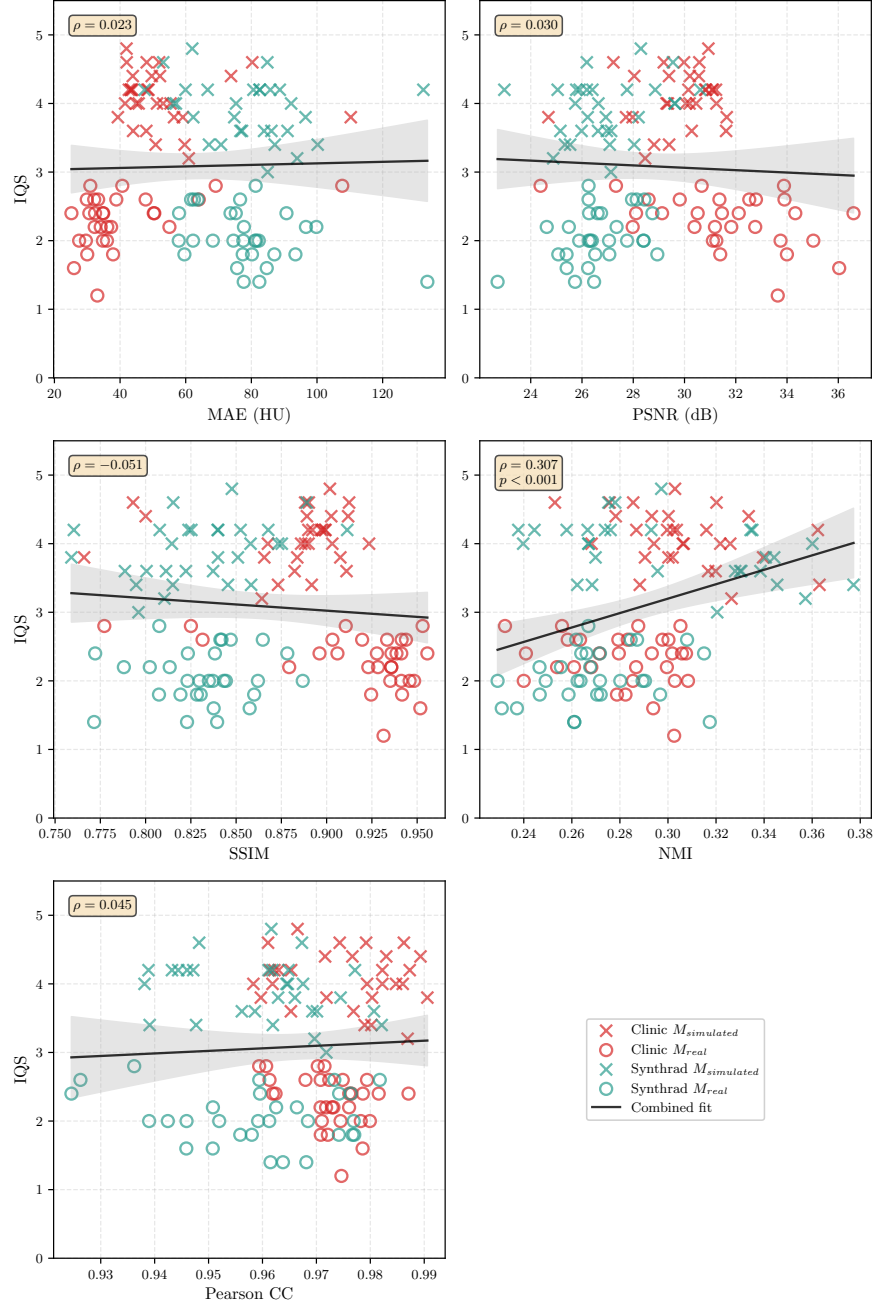


Figure 4: Relationship between quantitative metrics and clinical visual assessment scores. Green and red markers show samples from SynthRAD and Clinical datasets, respectively. Circles indicate M_{real} and crosses show $M_{simulated}$ samples. Note the inverted MAE-IQS relationship for Clinical data (red markers) compared to SynthRAD (green markers).

models, and reported performance gains may partially reflect better registration bias matching rather than better anatomical reconstruction. Clinical utility, as reflected in our IQS results, aligns with geometric fidelity rather than intensity metrics, suggesting current benchmarks inadequately capture clinical value.

The dataset-specific correlation analysis provided direct evidence for this concern. For the clinical dataset employing deformable registration, intensity metrics exhibited inverted correlations with IQS. Higher MAE was associated with higher clinical ratings ($\rho = 0.57$), while higher PSNR and SSIM were associated with lower ratings ($\rho = -0.46$ and -0.59 , respectively). This inversion occurred because deformable registration introduces spatial errors into the ground truth. Models minimizing MAE learn to reproduce these errors [20], yielding outputs that score well on benchmarks but were rated poorly by observers. For the SynthRAD dataset with rigid registration, intensity metrics showed no significant correlation with clinical preference, rendering them uninformative rather than misleading. The near-zero correlations observed in the combined analysis result from these opposing dataset-specific effects cancel out, which may obscure metric validity issues in multi-site studies with heterogeneous registration pipelines [7, 21]. In contrast, NMI maintained consistent positive correlation with IQS across both datasets ($\rho = 0.29$ and 0.31), supporting its use as a registration-bias-robust evaluation metric.

These observations have implications for model evaluation and benchmark design. Current challenges such as SynthRAD [12] employ consistent registration pipelines across training and validation sets, which may inadvertently reward models that learn registration-specific biases rather than true anatomical transformations. For clinical applications requiring accurate image registration, such as dose accumulation, structure propagation, treatment response assessment or structure segmentation, geometric fidelity may be more important than intensity accuracy alone [22, 23, 24]. Current state-of-the-art methods reported excellent intensity metrics (HUDiff: MAE 23.31 HU for brain and 26.11 HU for H&N [25]; TransCBCT: MAE 28.8 HU for prostate [26]), but geometric alignment was rarely evaluated, potentially masking clinically significant spatial errors.

The quality of ground truth data represents a fundamental, often overlooked factor limiting supervised sCT generation. Clinical CBCT/CT pairs

are rarely perfectly aligned due to inter-session variations in patient positioning and anatomy, forcing reliance on registration algorithms that introduce residual spatial errors. Our physics-based sCBCT generation framework addresses this limitation by providing perfectly aligned training pairs by construction.

Boussot *et al.* [20] observed analogous "registration bias" effects across multiple anatomical sites, finding that models trained with imperfect alignment achieved higher challenge scores precisely because evaluation employed the same registration strategy, directly supporting our findings (see Figure 3).

Inter-rater reliability for absolute IQS was limited (Table 5), reflecting the subjective nature of image quality assessment and varying emphasis on different quality dimensions among observers [27]. However, the strong consensus in preference (87% favoring $M_{\text{simulated}}$, average IQS 3.94 versus 2.04) indicated that despite variability in absolute scoring, the relative superiority of geometrically-faithful outputs was clinically perceptible. Observers consistently preferred outputs preserving anatomical relationships over those with lower intensity error but degraded spatial fidelity, suggesting geometric accuracy aligns with clinical intuition in ways intensity metrics alone do not capture. Based on these findings, we recommend incorporating geometric alignment metrics, evaluated against input images rather than registered ground truth, as standard evaluation criteria for sCT synthesis. However, geometric alignment metrics have limitations; they will fail to penalize intensity artifacts that do not affect spatial correspondence. Further investigation of evaluation metrics capturing both geometric fidelity and intensity accuracy without dependence on ground truth quality is warranted.

Several limitations should be acknowledged. The heuristic scatter model was empirically tuned for Elekta XVI imaging system and may require adjustment for other systems. The sinusoidal respiratory motion model may inadequately represent irregular breathing patterns and was currently also limited to the pelvic region. Clinical validation was limited to a single institution and gynecological cohort; generalization to other vendors and anatomical sites requires further investigation which is planned for follow-up work as well as the support for more body regions such as the abdomen and the thorax. Critically, while we demonstrated improved geometric alignment, downstream dosimetric impact was not directly evaluated which is an essential next step for establishing clinical utility.

The framework’s ability to generate unlimited geometrically-aligned training data offers practical advantages. Institutions can create site-specific datasets from planning data archives without paired CBCT acquisitions. The M_{finetune} results demonstrated that simulated pretraining provided useful initialization refinable with limited real data. Furthermore, our framework extends naturally to segmentation, reconstruction, and registration tasks where ground truth is similarly constrained by registration quality and missing label datasets.

6. Conclusion

This study demonstrated that physics-based sCBCT generation provides a viable solution to the registration problem limiting supervised sCT synthesis approaches. By eliminating registration errors through simulation, our framework enabled training with perfect geometric correspondence, resulting in models that preserve spatial relationships more accurately than those trained on registered clinical pairs. The consistent geometric alignment advantages observed across two independent datasets, combined with strong clinical observer preference for simulation-trained model outputs, support the utility of this approach for adaptive radiotherapy applications where spatial accuracy is of outmost importance. The computational efficiency of the framework enabled practical large-scale dataset generation, providing a foundation for further development of geometrically-faithful sCT synthesis methods.

Author Contributions

Lukas Zimmermann: Conceptualization, Data curation, Software, Formal analysis, Methodology, Writing – original draft

Michael Rauter: Software, Formal analysis, Methodology, Writing – original draft

Dietmar Georg: Writing – review and editing

Barbara Knäusl: Writing – review and editing, Funding acquisition, supervision project, administration

Maximilian Schmid: Writing – review and editing, Funding acquisition

Funding

The financial support by the Austrian Federal Ministry of Economy, Energy and Tourism, the National Foundation for Research, Technology and Development and the Christian Doppler Research Association is gratefully acknowledged. Michael Rauter was funded as part of the RTI-strategy Lower Austria 2027.

Acknowledgments

The authors thank the high performance computing team at the Medical University of Vienna for providing computational resources. We acknowledge the five independent observers (Data scientists = Lukas Zimmermann and Michael Rauter, Medical Physicists: Barbara Knäusl and Martin Buschmann, Radiation technologist = Kerstin Feichtinger) who participated in the visual analogue score assessment. We also thank the SynthRAD Challenge organizers for making the multi-institutional dataset available.

Declaration of generative AI and AI-assisted technologies in the manuscript preparation process

During the preparation of this work the author(s) used claude.ai in order to improve writing and grammar. After using this tool/service, the author(s) reviewed and edited the content as needed and take(s) full responsibility for the content of the published article.

Appendix A. Ablation study

We performed an ablation study for adjustable parameters: saturation factor c_{sat} , breathing amplitude A_{max} , scatter-to-primary ratio SPR and photon flux Φ . Although Φ and SPR was known for the Elekta XVI system, we evaluated whether the nominal value was optimal for our simulation framework. Each parameter was varied independently while holding others at their default values, evaluated across n=10 patients (Table A.1).

Optimal FID and MMD were achieved with $c_{sat} = 2.0$ and $A_{max} = 5$ mm. The nominal photon flux ($\Phi = 4.16 \times 10^5$) performed comparably to higher values, with MMD favoring the nominal setting while FID/MMD showed marginal improvement at $\Phi = 6.0 \times 10^5$ and $SPR = 0.5$; we retained the physically measured value. Notably, disabling motion simulation ($A_{max} = 0$

Table A.1: Ablation study results with FID and MMD across n=10 patients.

Configuration	FID ↓	MMD ↓
<i>Saturation Factor</i> ($\Phi = 4.16 \times 10^5$, $A_{max} = 5$ mm, $SPR = 1.6$)		
$c_{sat} = 1.0$	69.47	2.16
$c_{sat} = 1.5$	68.47	1.52
$c_{sat} = 2.0$	63.62	1.10
<i>Photon Flux</i> ($c_{sat} = 2.0$, $A_{max} = 5$ mm, $SPR = 1.6$)		
$\Phi = 2.0 \times 10^5$	66.67	1.38
$\Phi = 4.16 \times 10^5$	63.20	1.11
$\Phi = 6.0 \times 10^5$	62.66	1.11
<i>Breathing Amplitude</i> ($c_{sat} = 2.0$, $\Phi = 4.16 \times 10^5$, $SPR = 1.6$)		
$A_{max} = 0$ mm	71.00	1.43
$A_{max} = 5$ mm	63.41	1.12
$A_{max} = 10$ mm	70.04	1.38
<i>Scatter-to-Primary Ratio</i> ($c_{sat} = 2.0$, $\Phi = 4.16 \times 10^5$, $A_{max} = 5$ mm)		
$SPR = 0.5$	64.77	1.10
$SPR = 1.6$	63.57	1.11
$SPR = 2.5$	66.03	1.36

mm) substantially degraded realism (FID: 71.00 vs 63.41), confirming that respiratory motion modeling is necessary for generating realistic simulated CBCT images.

References

- [1] O. M. Dona Lemus, M. Cao, B. Cai, M. Cummings, D. Zheng, Adaptive radiotherapy: Next-generation radiotherapy, *Cancers* 16 (6) (2024) 1206. [doi:10.3390/cancers16061206](https://doi.org/10.3390/cancers16061206)
URL <https://doi.org/10.3390/cancers16061206>
- [2] R. Schulze, U. Heil, D. Gross, D. Bruellmann, E. Dranischnikow, U. Schwancke, E. Schoemer, Artefacts in cbct: a review, *Dentomaxillofacial Radiology* 40 (5) (2011) 265–273. [doi:10.1259/dmfr/30642039](https://doi.org/10.1259/dmfr/30642039).
URL <https://doi.org/10.1259/dmfr/30642039>
- [3] M. Rabe, C. Kurz, A. Thummerer, G. Landry, Artificial intelligence for treatment delivery: image-guided radiotherapy (3 2025). [doi:10.1007/s00066-024-02277-9](https://doi.org/10.1007/s00066-024-02277-9).
- [4] S. Dayarathna, K. T. Islam, S. Uribe, G. Yang, M. Hayat, Z. Chen, Deep learning based synthesis of mri, ct and pet: Review and analysis, *Medical Image Analysis* 92 (2024) 103046. [doi:https://doi.org/10.1016/j.media.2023.103046](https://doi.org/10.1016/j.media.2023.103046).
URL <https://www.sciencedirect.com/science/article/pii/S1361841523003067>
- [5] A. Thummerer, E. van der Bijl, A. Galapon, J. J. Verhoeff, J. A. Langendijk, S. Both, C. N. A. van den Berg, M. Maspero, Synthrad2023 grand challenge dataset: Generating synthetic ct for radiotherapy, *Medical Physics* 50 (2023) 4664–4674. [doi:10.1002/mp.16529](https://doi.org/10.1002/mp.16529).
- [6] A. Thummerer, E. van der Bijl, A. J. Galapon, F. Kamp, M. Savenije, C. Muijs, S. Aluwini, R. J. Steenbakkers, S. Beuel, M. P. Intven, J. A. Langendijk, S. Both, S. Corradini, V. Rogowski, M. Terpstra, N. Wahl, C. Kurz, G. Landry, M. Maspero, Synthrad2025 grand challenge dataset: Generating synthetic cts for radiotherapy from head to abdomen, *Medical Physics* 52 (7 2025). [doi:10.1002/mp.17981](https://doi.org/10.1002/mp.17981).

[7] L. Nenoff, F. Amstutz, M. Murr, B. Archibald-Heeren, M. Fusella, M. Hussein, W. Lechner, Y. Zhang, G. Sharp, E. Vasquez Osorio, Review and recommendations on deformable image registration uncertainties for radiotherapy applications, *Physics in Medicine and Biology* 68 (24) (2023) 24TR01. doi:10.1088/1361-6560/ad0d8a.

[8] C. Suwanraksa, J. Bridhikitti, T. Liamsuwan, S. Chaichulee, Cbct-to-ct translation using registration-based generative adversarial networks in patients with head and neck cancer, *Cancers* 15 (7) (2023). doi: 10.3390/cancers15072017.
URL <https://www.mdpi.com/2072-6694/15/7/2017>

[9] X. Liang, L. Chen, D. Nguyen, Z. Zhou, X. Gu, M. Yang, J. Wang, S. Jiang, Generating synthesized computed tomography (ct) from cone-beam computed tomography (cbct) using cyclegan for adaptive radiation therapy, *Physics in Medicine & Biology* 64 (12) (2019) 125002. doi: 10.1088/1361-6560/ab22f9.
URL <https://doi.org/10.1088/1361-6560/ab22f9>

[10] Y. Liu, Y. Lei, T. Wang, Y. Fu, X. Tang, W. J. Curran, T. Liu, P. Patel, X. Yang, CBCT-based synthetic CT generation using deep-attention cycleGAN for pancreatic adaptive radiotherapy, *Medical Physics* 47 (6) (2020) 2472–2483. doi:10.1002/mp.14121.

[11] Y. Hu, M. Cheng, H. Wei, Z. Liang, A joint learning framework for multisite cbct-to-ct translation using a hybrid cnn-transformer synthesizer and a registration network, *Frontiers in Oncology* Volume 14 - 2024 (2024). doi:10.3389/fonc.2024.1440944.
URL <https://www.frontiersin.org/journals/oncology/articles/10.3389/fonc.2024.1440944>

[12] E. M. Huijben, M. L. Terpstra, A. J. Galapon, S. Pai, A. Thummerer, P. Koopmans, M. Afonso, M. van Eijnatten, O. Gurney-Champion, Z. Chen, Y. Zhang, K. Zheng, C. Li, H. Pang, C. Ye, R. Wang, T. Song, F. Fan, J. Qiu, Y. Huang, J. Ha, J. Sung Park, A. Alain-Beaudoin, S. Bériault, P. Yu, H. Guo, Z. Huang, G. Li, X. Zhang, Y. Fan, H. Liu, B. Xin, A. Nicolson, L. Zhong, Z. Deng, G. Müller-Franzes, F. Khader, X. Li, Y. Zhang, C. Hémon, V. Boussot, Z. Zhang, L. Wang, L. Bai, S. Wang, D. Mus, B. Kooiman, C. A. Sargeant,

E. G. Henderson, S. Kondo, S. Kasai, R. Karimzadeh, B. Ibragimov, T. Helfer, J. Dafflon, Z. Chen, E. Wang, Z. Perko, M. Maspero, Generating synthetic computed tomography for radiotherapy: Synthrad2023 challenge report, *Medical Image Analysis* 97 (2024) 103276. [doi:
https://doi.org/10.1016/j.media.2024.103276](https://doi.org/10.1016/j.media.2024.103276).
URL <https://www.sciencedirect.com/science/article/pii/S1361841524002019>

[13] M. Unberath, J.-N. Zaech, S. C. Lee, B. Bier, J. Fotouhi, M. Armand, N. Navab, DeepDRR—A Catalyst for Machine Learning in Fluoroscopy-guided Procedures, in: *Proc. Medical Image Computing and Computer Assisted Intervention (MICCAI)*, Springer.

[14] Y. Pang, Y. Liu, X. Chen, P.-T. Yap, J. Lian, Sinosynth: A physics-based domain randomization approach for generalizable cbct image enhancement, in: M. G. Linguraru, Q. Dou, A. Feragen, S. Giannarou, B. Glocker, K. Lekadir, J. A. Schnabel (Eds.), *Medical Image Computing and Computer Assisted Intervention – MICCAI 2024*, Springer Nature Switzerland, Cham, 2024, pp. 646–656.

[15] M. Unberath, J.-N. Zaech, C. Gao, B. Bier, F. Goldmann, S. C. Lee, J. Fotouhi, R. Taylor, M. Armand, N. Navab, Enabling Machine Learning in X-ray-based Procedures via Realistic Simulation of Image Formation, *International journal of computer assisted radiology and surgery (IJCARS)* (2019).

[16] S. Rit, M. Vila Oliva, S. Brousmiche, R. Labarbe, D. Sarrut, G. C. Sharp, The reconstruction toolkit (rtk), an open-source cone-beam ct reconstruction toolkit based on the insight toolkit (itk), *Journal of Physics: Conference Series* 489 (1) (2014) 012079. [doi:
10.1088/1742-6596/489/1/012079](https://doi.org/10.1088/1742-6596/489/1/012079).
URL <https://doi.org/10.1088/1742-6596/489/1/012079>

[17] S. Klein, M. Staring, K. Murphy, M. A. Viergever, J. P. Pluim, elastix: a toolbox for intensity based medical image registration, *IEEE Transactions on Medical Imaging* 29 (1) (2010) 196–205. [doi:
10.1109/TMI.2009.2035616](https://doi.org/10.1109/TMI.2009.2035616).

[18] V. Boussot, C. Hémon, J.-C. Nunes, J. Dowling, S. Rouzé, C. Lafond, A. Barateau, J.-L. Dillenseger, Impact: A generic semantic loss for mul-

timodal medical image registration (2025). [arXiv:2503.24121](https://arxiv.org/abs/2503.24121).
URL <https://arxiv.org/abs/2503.24121>

[19] F. Isensee, P. F. Jaeger, S. A. Kohl, J. Petersen, K. H. Maier-Hein, nnU-Net: a self-configuring method for deep learning-based biomedical image segmentation, *Nature Methods* 18 (2) (2021) 203–211.
URL <http://dx.doi.org/10.1038/s41592-020-01008-z>

[20] V. Boussot, C. Hémon, J.-C. Nunes, J.-L. Dillenseger, Why registration quality matters: Enhancing sct synthesis with impact-based registration (2025). [arXiv:2510.21358](https://arxiv.org/abs/2510.21358).
URL <https://arxiv.org/abs/2510.21358>

[21] T. Rohlffing, Image similarity and tissue overlaps as surrogates for image registration accuracy: widely used but unreliable, *IEEE Transactions on Medical Imaging* 31 (2) (2012) 153–163. [doi:10.1109/TMI.2011.2163944](https://doi.org/10.1109/TMI.2011.2163944).

[22] I. J. Chetty, M. Rosu-Bubulac, Deformable registration for dose accumulation, *Seminars in Radiation Oncology* 29 (3) (2019) 198–208. [doi:10.1016/j.semradonc.2019.02.002](https://doi.org/10.1016/j.semradonc.2019.02.002).

[23] E. Brion, J. Léger, A. Barragán-Montero, N. Meert, J. A. Lee, B. Macq, Domain adversarial networks and intensity-based data augmentation for male pelvic organ segmentation in cone beam ct, *Computers in Biology and Medicine* 131 (2021) 104269. [doi:https://doi.org/10.1016/j.combiomed.2021.104269](https://doi.org/10.1016/j.combiomed.2021.104269).
URL <https://www.sciencedirect.com/science/article/pii/S0010482521000639>

[24] A. Belfatto, M. Riboldi, D. Ciardo, A. Cecconi, R. Lazzari, B. Jereczek-Fossa, R. Orecchia, G. Baroni, P. Cerveri, Adaptive mathematical model of tumor response to radiotherapy based on cbct data, *IEEE Journal of Biomedical and Health Informatics* 20 (3) (2016) 802–809. [doi:10.1109/JBHI.2015.2453437](https://doi.org/10.1109/JBHI.2015.2453437).

[25] C. Hu, N. Cao, X. Li, Y. He, H. Zhou, CBCT-to-CT synthesis using a hybrid U-Net diffusion model based on transformers and information bottleneck theory, *Scientific Reports* 15 (1) (2025) 10816. [doi:10.1038/s41598-025-13740-0](https://doi.org/10.1038/s41598-025-13740-0)

s41598-025-92094-6.

URL <https://doi.org/10.1038/s41598-025-92094-6>

- [26] X. Chen, Y. Liu, B. Yang, J. Zhu, S. Yuan, X. Xie, Y. Liu, J. Dai, K. Men, A more effective CT synthesizer using transformers for cone-beam CT-guided adaptive radiotherapy, *Frontiers in Oncology* 12 (2022) 988800. doi:10.3389/fonc.2022.988800.
- [27] L. Flight, S. A. Julious, The disagreeable behaviour of the kappa statistic, *Pharmaceutical Statistics* 14 (1) (2015) 74–78. doi:10.1002/pst.1659.